Acoustics in Porous Media.

JUAN E. SANTOS[†]

work in collaboration with

J. M. Carcione, S. Picotti, P. M. Gauzellino and R. Martinez Corredor.

[†] Department of Mathematics, Purdue University, W. Lafayette, Indiana, and CONICET, Instituto del Gas y del Petróleo, Facultad de Ingeniería Universidad de Buenos Aires, and Universidad Nacional de La Plata, Argentina

Institute of Acoustics Orso Mario Corbino July 19th, 2013

Introduction.

- The acoustics of fluid-saturated porous media is an active area of research in many fields, such as seismic exploration, petroleum reservoir characterization and monitoring, CO_2 sequestration and nondestructive testing of materials by ultrasonic methods.
- M. A. Biot (JASA, 1956; J. Appl. Physics, 1962) developped a theory for wave propagation in a porous medium saturated by a single-phase fluid, showing the existence of two compressional waves (P1, P2 waves) and one shear wave. Plona (Appl. Phys. Lett., 1980) was the first to observe the P2 wave in the laboratory.
- Numerical simulation based on Biot's theory is a useful tool to characterize this multiphasic materials.

A representative sample of a porous medium

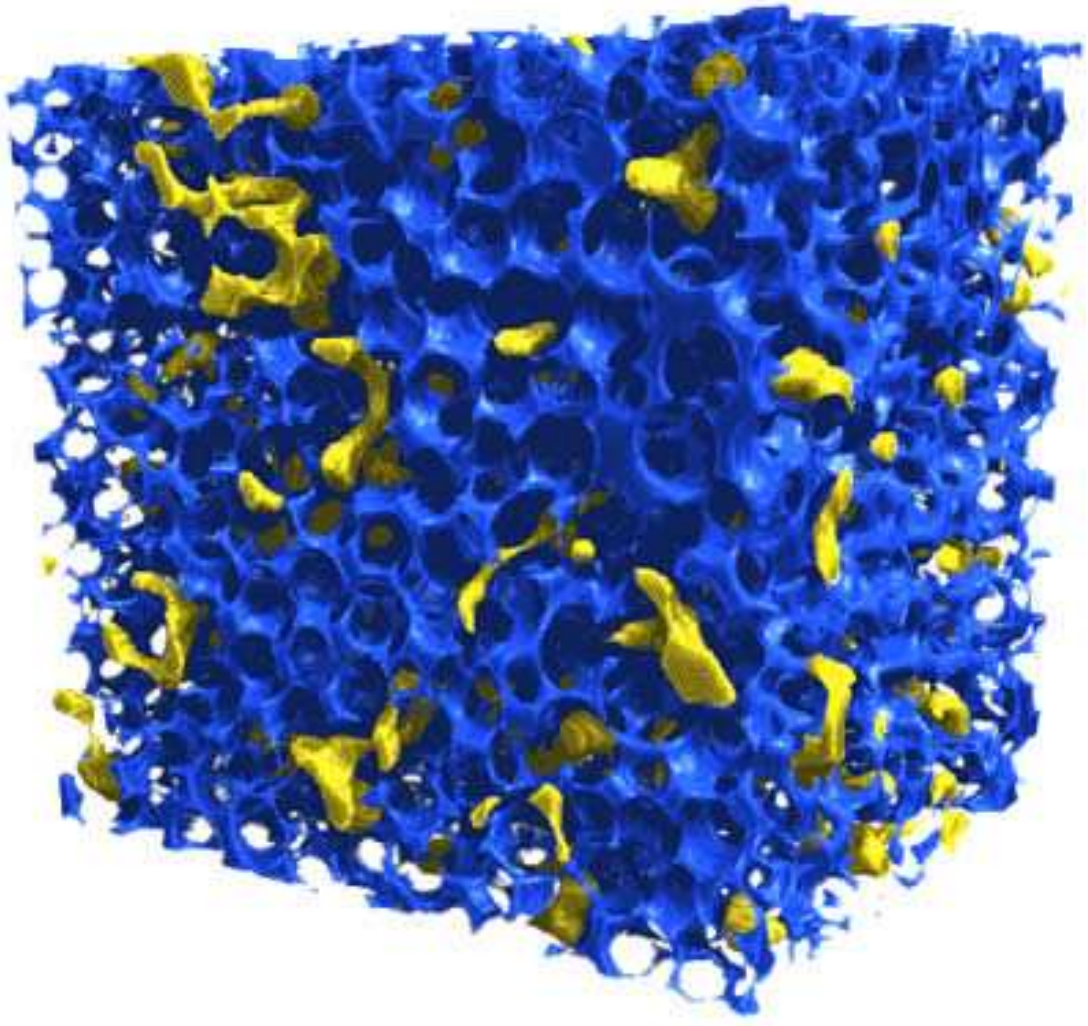

Blue regions represent water, yellow regions hydrocarbon and the void spaces the solid matrix.

The Biot Model.

V_b : **volume of homogeneous** *bulk material* **of effective porosity** ϕ **containing a** *pore volume* V_p **completely saturated by a single-phase fluid:**

$$\phi = \frac{V_p}{V_b}$$

$u^{(s)}$, $\widetilde{u}^{(f)}$, : **time Fourier transform of the averaged displacement vectors of the solid and fluid phases, respectively.**

$$u^{(f)} = \phi(\widetilde{u}^{(f)} - u^{(s)}), \qquad u = (u^{(s)}, u^{(f)}).$$

σ_{ij}: **time Fourier transform of the total stress tensor of the bulk material,**

p_f: **time Fourier transform of the fluid pressure,**

ε_{ij} : **time Fourier transform of the strain tensor of the solid.**

Constitutive Relations.

$$\sigma_{ij}(u) = 2\mu\,\varepsilon_{ij}(u^{(s)}) + \delta_{ij}(\lambda_c \nabla \cdot u^{(s)} + \alpha K_{av}\,\nabla \cdot u^{(f)}),$$

$$p_f(u) = -\alpha K_{av}\,\nabla \cdot u^{(s)} - K_{av}\,\nabla \cdot u^{(f)},$$

where

$$\alpha = 1 - \frac{K_m}{K_s}, \quad K_{av} = \left[\frac{\alpha - \phi}{K_s} + \frac{\phi}{K_f}\right]^{-1}.$$

$$K_G = K_m + \alpha^2 K_{av} \quad \lambda_G = K_G - \frac{2}{3}\mu,$$

μ**: shear modulus of the dry matrix,**

K_m, Ks, K_f, K_G**: bulk modulus of the dry matrix, the solid grains, the saturant fluid, and the saturated bulk material, respectively.**

Biot's Equations of Motion.

$$-\omega^2 \rho u^{(s)} - \omega^2 \rho_f u^{(f)} - \nabla \cdot \sigma(u) = F^{(s)}$$

$$-\omega^2 \rho_f u^{(s)} - \omega^2 g u^{(f)} + i\omega \frac{\eta}{\kappa} u^{(f)} + \nabla p_f(u) = F^{(f)}.$$

ω: **angular frequency**

$\rho = (1-\phi)\rho_s + \phi\rho_f$: **bulk modulus**

ρ_f, ρ_s: **mass densities of the fluid and the solid grains,**

g : **mass coupling parameters**

η: **Fluid viscosity,** κ: **Permeability,**

Plane Wave Analysis

In these type of media, two compressional waves (P_1, P_2) and one shear wave (or S)-wave) can propagate.

P_1 and S waves: analogues of the classical fast waves propagating in elastic or viscoelastic isotropic solids.

P_2 wave: slow diffusion type wave in the low frequency range and a truly propagating mode in the ultrasonic range.

The P_2 wave is due to the motions out of phase of the solid and fluid phases.

P_2 waves are generated by conversion of the fast P_1 and S waves at interfaces within heterogeneous poroelastic materials, causing attenuation and dispersion on the fast modes.

A Variational Formulation. 2D Case.

Ω : **rectangular domain**, $\quad \mathcal{V} = \left[H^1(\Omega)\right]^2 \times H(\mathbf{div}; \Omega)$**.**

Testing Biot's equation of motion with $v \in \mathcal{V}$ **we get the** *weak form***:**

$$-\omega^2 \left(\mathcal{P}u, v\right) + i\omega \left(\frac{\eta}{\kappa} u^{(f)}, v^{(f)}\right) + \mathcal{A}(u, v) + i\omega \left\langle \mathcal{D}u, v \right\rangle = (F, v),$$

$$v = \left(v^{(s)}, v^{(f)}\right)^t \in \mathcal{V},$$

$$\mathcal{A}(u, v) = \sum_{l,m} \left(\sigma_{lm}(u), \varepsilon_{lm}(v^{(s)})\right) - \left(p_f(u), \nabla \cdot v^{(f)}\right), \; u, v \in \mathcal{V}.$$

$$\mathcal{P} = \begin{pmatrix} \rho I & \rho_f I \\ \rho_f I & g I \end{pmatrix}, \qquad F = (F^{(s)}, F^{(f)}).$$

I**:identity matrix in** $R^{2\times 2}$ $\qquad$ $\mathcal{D}$ **: a positive definite matrix .**

The Finite Element Method (FEM). Rectangular Elements.

$$\mathcal{V}^h = \left[\mathcal{NC}^h\right]^2 \times \mathcal{W}^h$$

$\mathcal{NC}^h$: a nonconforming FE space used to approximate each component of the solid displacement vector.

$\mathcal{W}^h$: conforming FE space used to aproximate the fluid displacement.

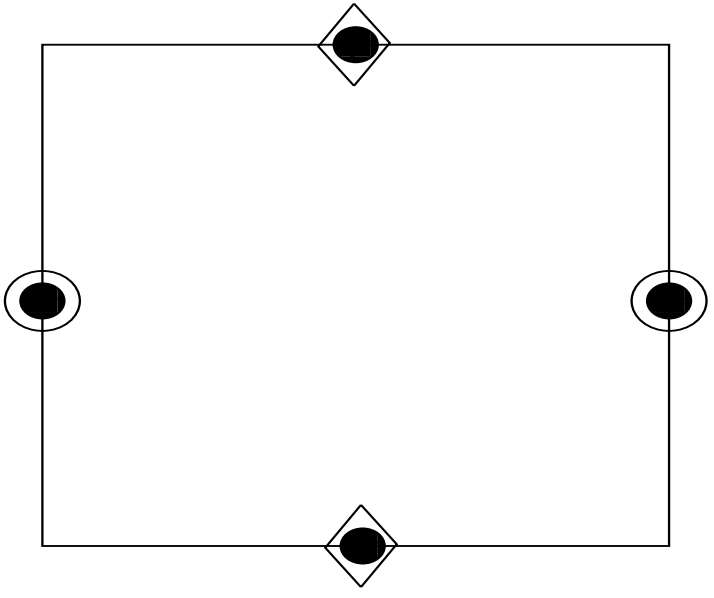

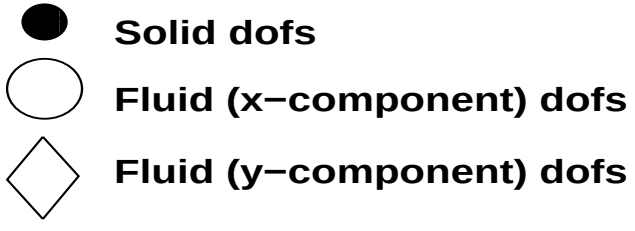

Local degrees of freedom (DOF's)

Applications. The Mesoscopic Loss Mechanism. I

- A major cause of seismic attenuation in porous media is wave-induced fluid flow, which occurs at mesoscopic scales.
- A fast P_1 wave induces a fluid-pressure difference at mesoscopic-scale inhomogeneities (larger than the pore size but smaller than the wavelength, typically tens of cen- timetres), generating fluid flow and slow (diffusion) P_2 Biot waves
- White (1975) was the first to show that mesoscopic loss can be observed in the seismic range in a sandstone with partial gas saturation.
- Next we show a numerical verification of the mesoscopic loss mechanism using the FEM.

Numerical Simulations to illustrate the mesoscopic loss mechanism.

The computational domain is a square of side length 800 m representing a poroelastic rock alternately saturated with gas and water.

The perturbation $F = (F^{(s)}, F^{(f)})$ is a compressional point source applied to the matrix, located inside the region at (x_s, y_s) = (400 m, 4 m) with (dominant) frequency 20 Hz.

Biot's equations of motion were solved for 110 temporal frequencies in the interval $(0, 60Hz)$ employing a FE domain decomposition iterative procedure.
The domain was discretized into square cells of side length $h = 40$ cm.

The time domain solution was obtained performing an approximate inverse Fourier transform.

Time histories for a porous rock saturated by gas (top left), water (top right) and periodic gas-water (bottom)

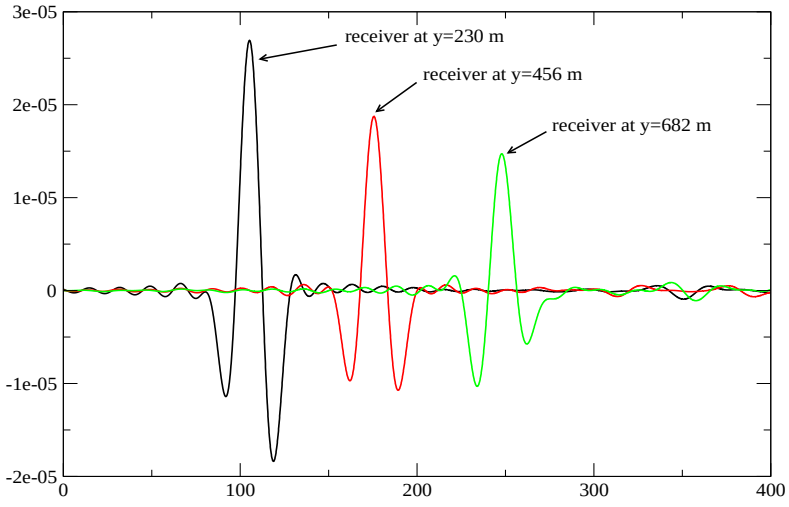

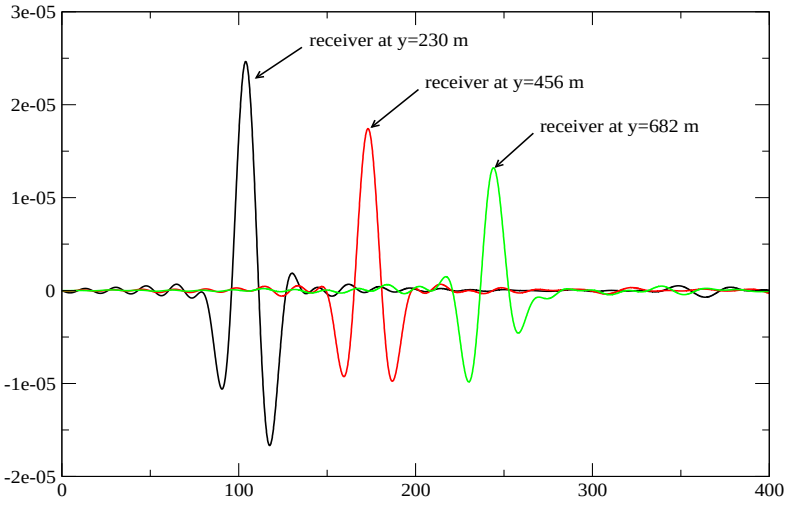

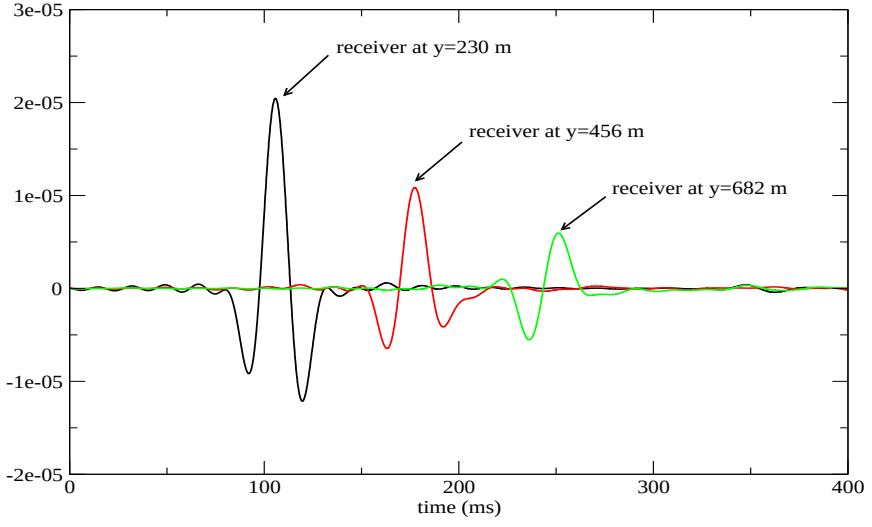

Time histories observed at a receiver for a porous rock saturated by gas, water and periodic gas-water.

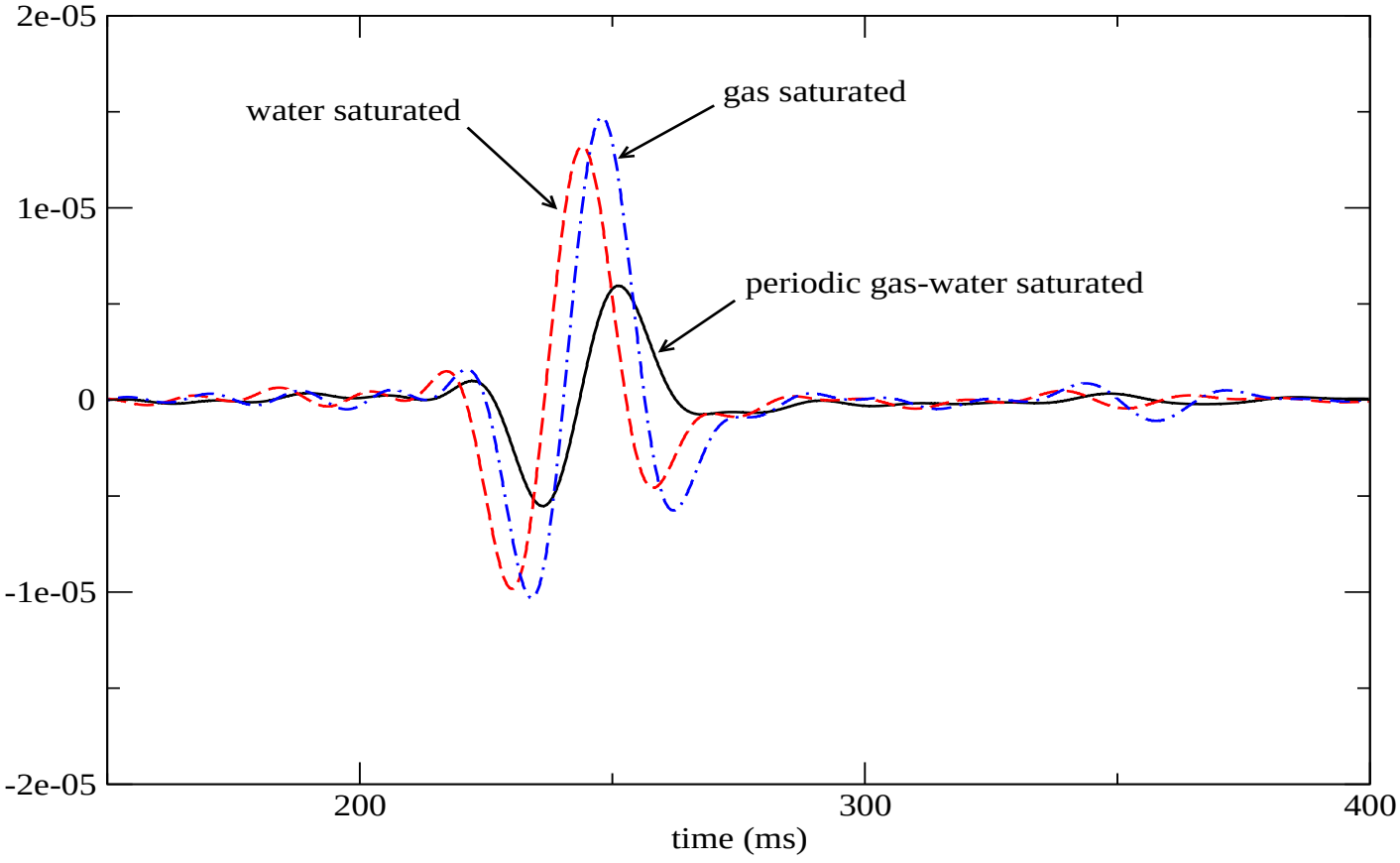

The delay in in the arrival time in the periodic gas-water case is due to the velocity dispersion caused by the mesoscopic scale heterogeneities. The associated attenuation is in agreement with that predicted by White's theory.

Extensions of Biot theory.

- A porous medium saturated by immiscible fluids. The theory was presented by Santos et al. (J. Acoust. Soc. Am., 1990a, b).
  In these type of media, three compressional waves (P_1, P_2, P_3 waves) and one shear wave (S wave) can propagate.
- A porous composite matrix saturated by a single-phase fluid. The theory was developped by Leclaire et al. (J. Acoust. Soc. Am., 1995) for the uniform porosity case and then extended to the more realistic variable porosity case by Carcione et al. (J. Appl. Physics, 2003) and Santos et a. (J. Acoust. Soc. Am., 2004).
  In this case 3 compressional waves (P_1, P_2, P_3 waves) and 2 shear waves (S_1, S_2 waves) can propagate. Observation of the slow waves were presented in Leclaire et al. (J. Acoust. Soc. Am., 1995).

The immiscible fluids model. Saturation interface. Snapshot of the solid phase z-velocity at $t = 0.007$ ms.

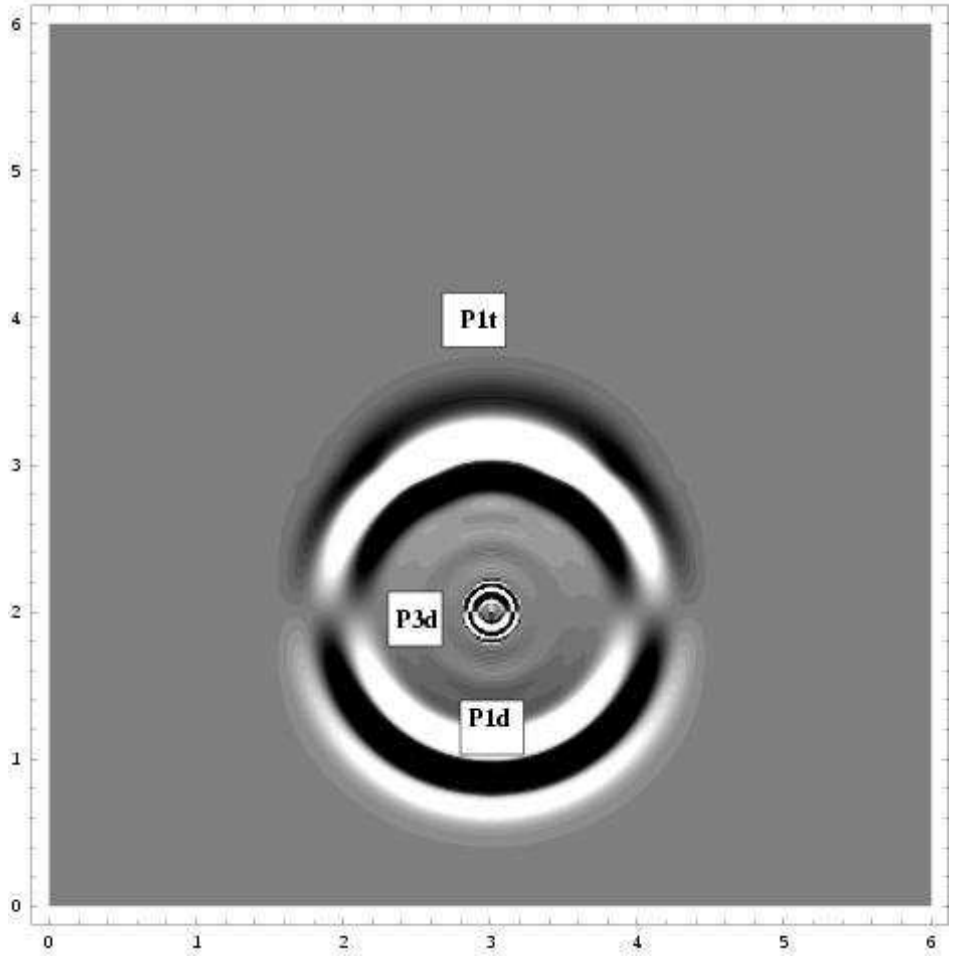

The interface divides the domain in two layers of equal thickness (3 cm). The lower layer (where the source is located) has nonwetting saturation S_n =0.9, while in the upper layer $S_n = 0.1$. A compressional point source of dominant frequency 500 kHz is located at $x = 3$ cm, $z = 2$ cm.

Saturation interface. Snapshot of the solid phase z-velocity at $t = 0.012$ ms

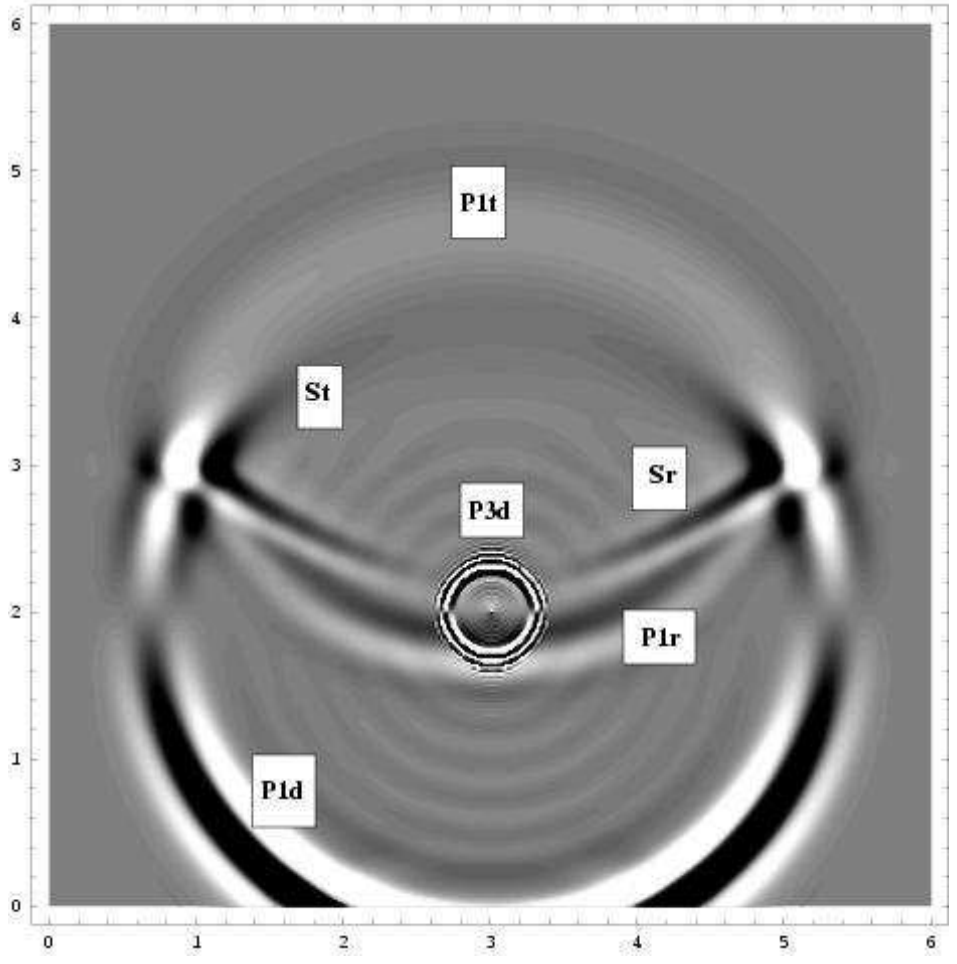

Amplitude of wavefronts measured with respect to amplitude of incident P_{1d} wavefront:

$$A(P_{1r}) \approx 0.06,\ A(S_r) \approx 0.09,\ A(S_t) \approx 0.29,\ A(P_{1t}) \approx 0.2$$

Saturation interface. Snapshot of the solid phase z-velocity at $t = 0.045$ ms

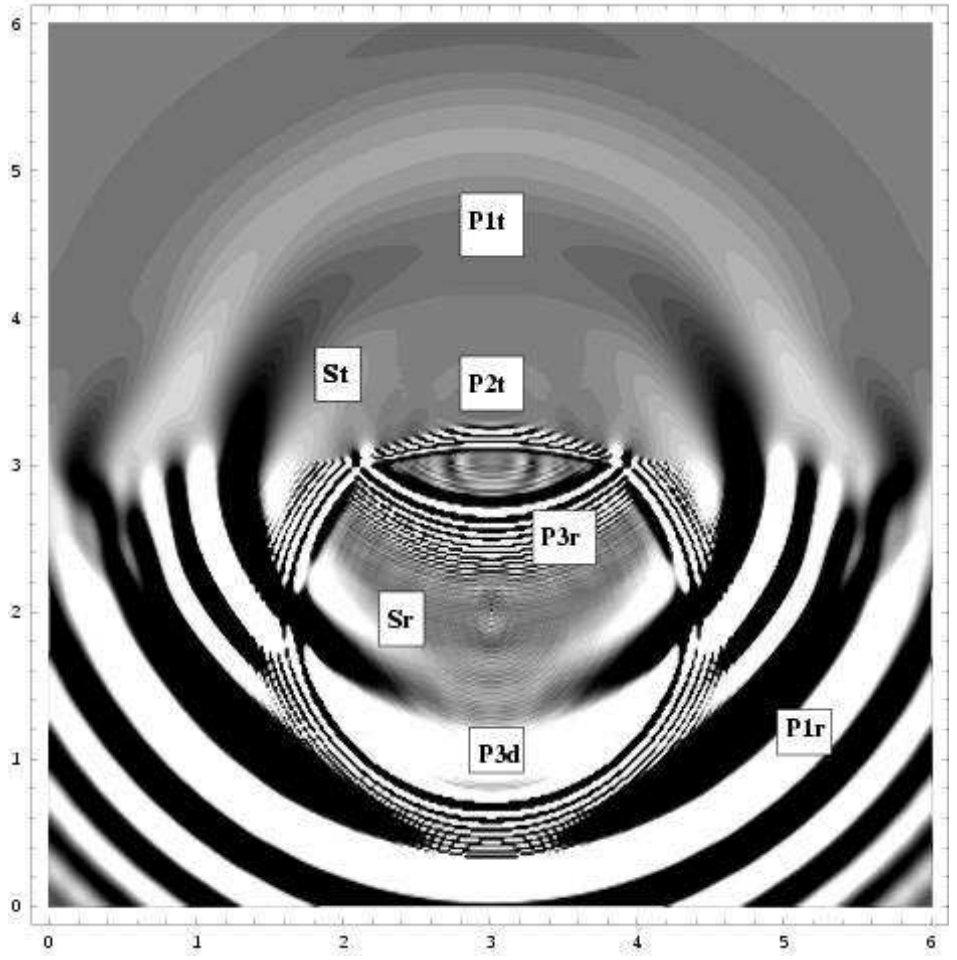

Amplitude of wavefronts measured with respect to amplitude of incident P_{3d} wavefront:

$A(P_{1r}) \approx 0.1$, $A(P_{3r}) \approx 0.122$, $A(S_r) \approx 0.044$, $A(P_{1t}) \approx 0.09$, $A(P_{2t}) \approx 0.055$, $A(S_t) \approx 0.006$

Patchy saturation map. White regions correspond to almost full gas saturation.

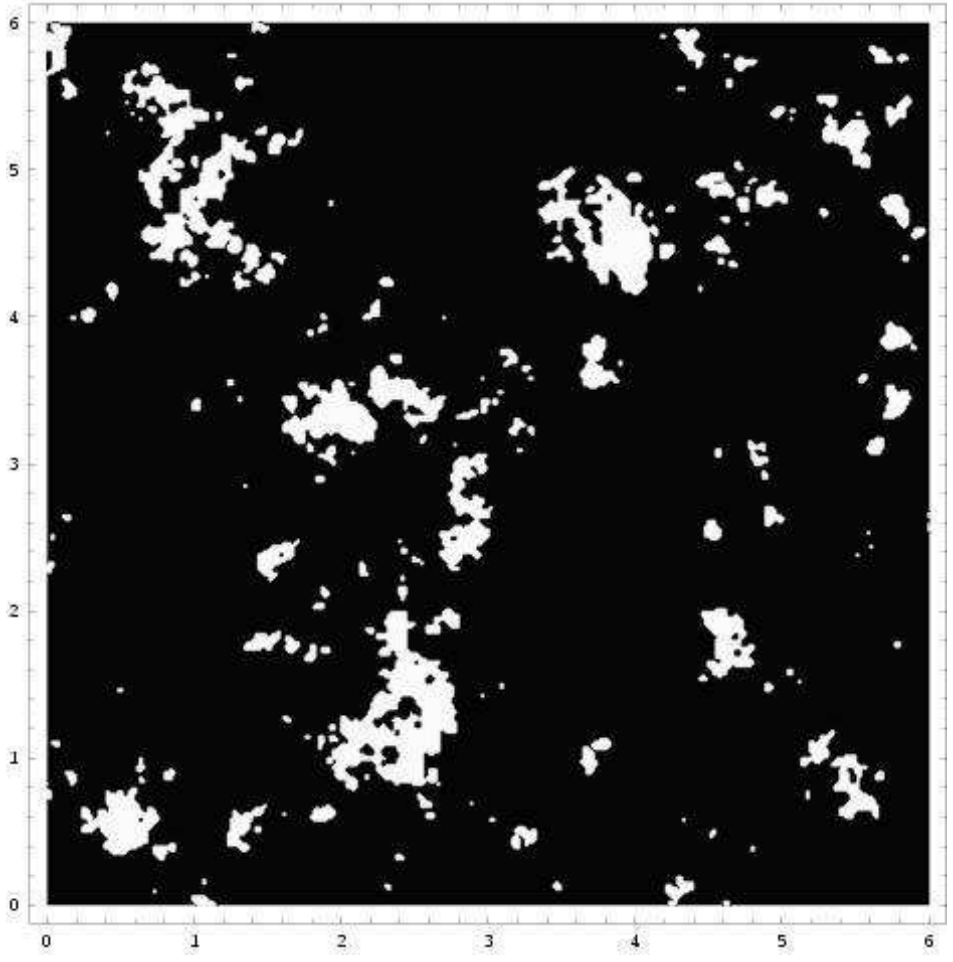

Macroscopic nonwetting saturation $S_n = 0.1$

Patchy saturation. Snapshot of the solid phase z-velocity at $t = 0.007$ ms

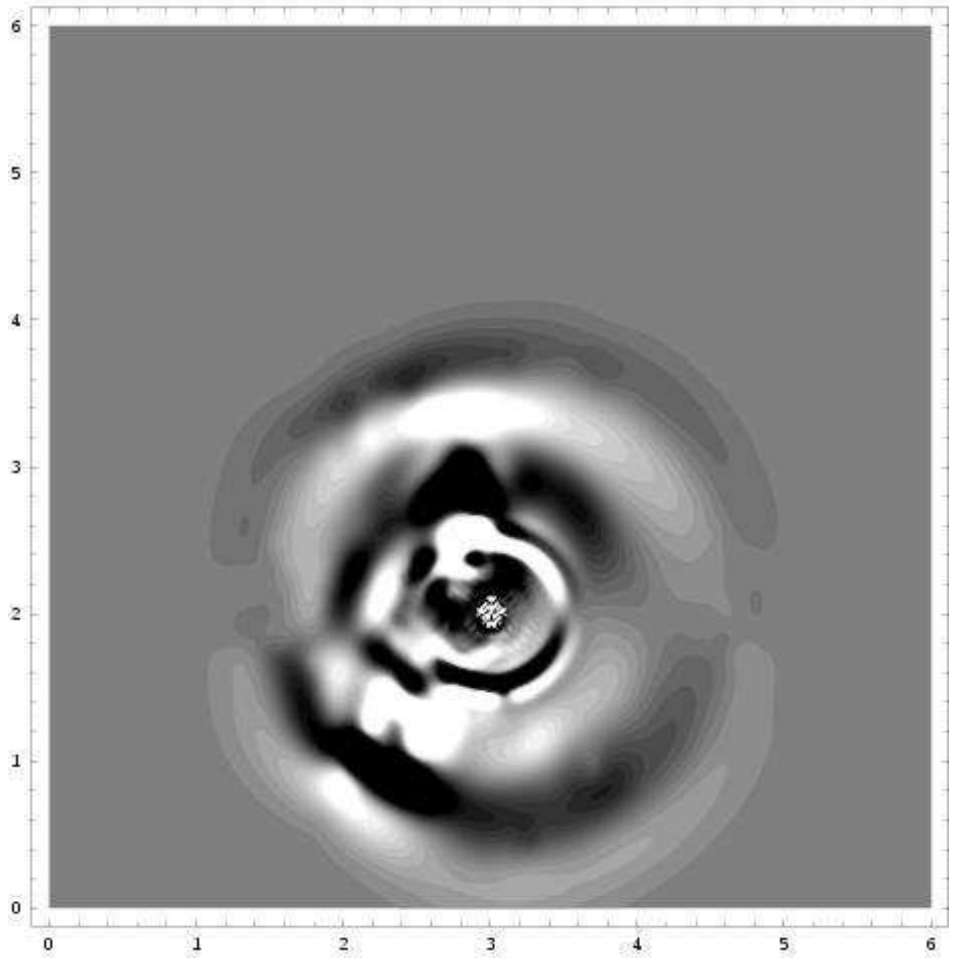

Irregular wavefronts are associated with compressional and shear waves generated at the gas patches. Thin wavefronts are associated with slow P_2, P_3 waves.

Patchy saturation. Curl of the velocity of the solid phase at $t = 0.007$ ms

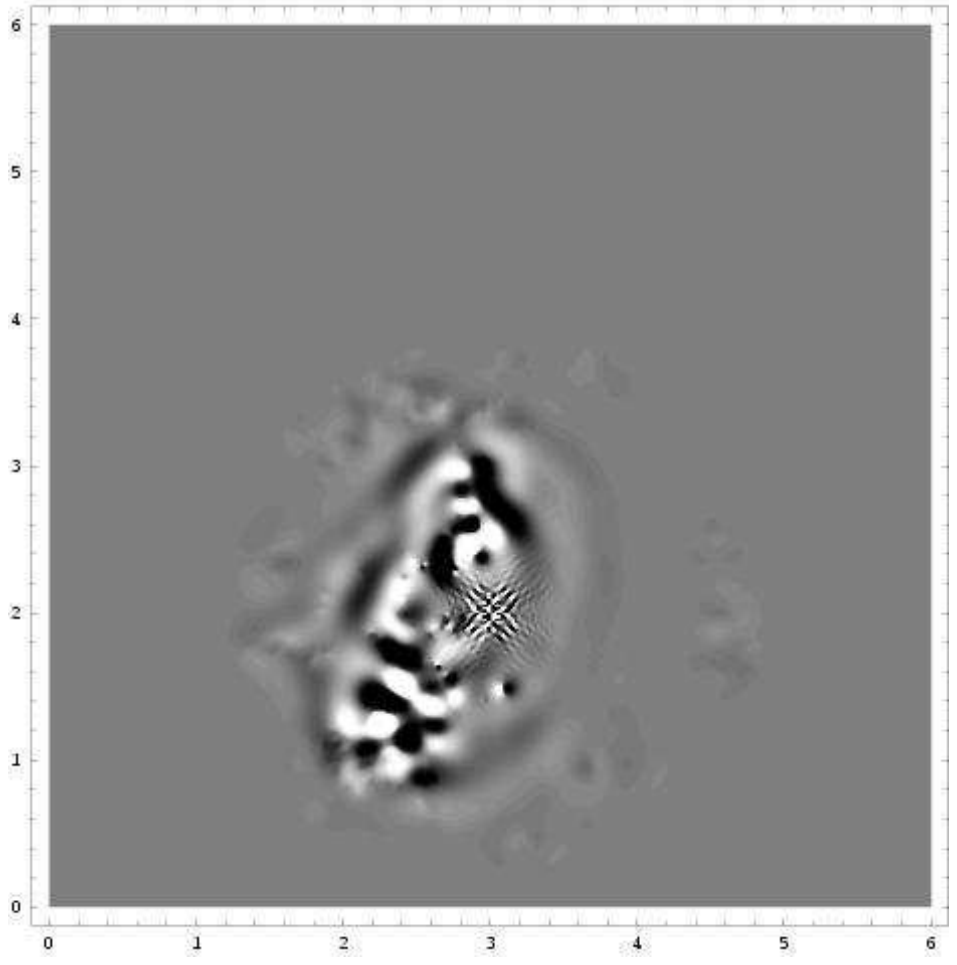

Shear waves are generated at the gas-water interfaces by mode conversion.

- **Gas hydrates (GH)** are crystalline molecular complexes composed of water and natural gas, mainly methane. They form under conditions of low temperature, high pressure and gas concentration and are observed in permafrost regions and seaflor sediments along the continental margins.
- **GH** are ice-like structures within the pore space that cause strong changes in the physical and mechanical properties of the rock, making possible to detect its presence using seismic data.
- The interest in **GH** bearing sediments GH is mainly due to their potential as future energy resources.

Wave Propagation in GH Bearing Sediments.

- Borehole sonic log and cross-hole tomography data from the Mallik field (Mackenzie Delta, Canada), indicate that attenuation **increases** with **GH content**.
- Slow-waves energy conversions take place when a fast (classical) seismic wave strikes an heterogeneity within the **GH** bearing sediments, generating slow compressional (P_2, P_3) and shear (S_2) waves.
- These scattering-type effects can explain the observed levels of attenuation in **GH-bearing sediments**, which is tested using numerical simulations.

GH saturation distribution. The domain is a square of side length 1.5 m. Overall GH saturation $S_{gh} = .58$

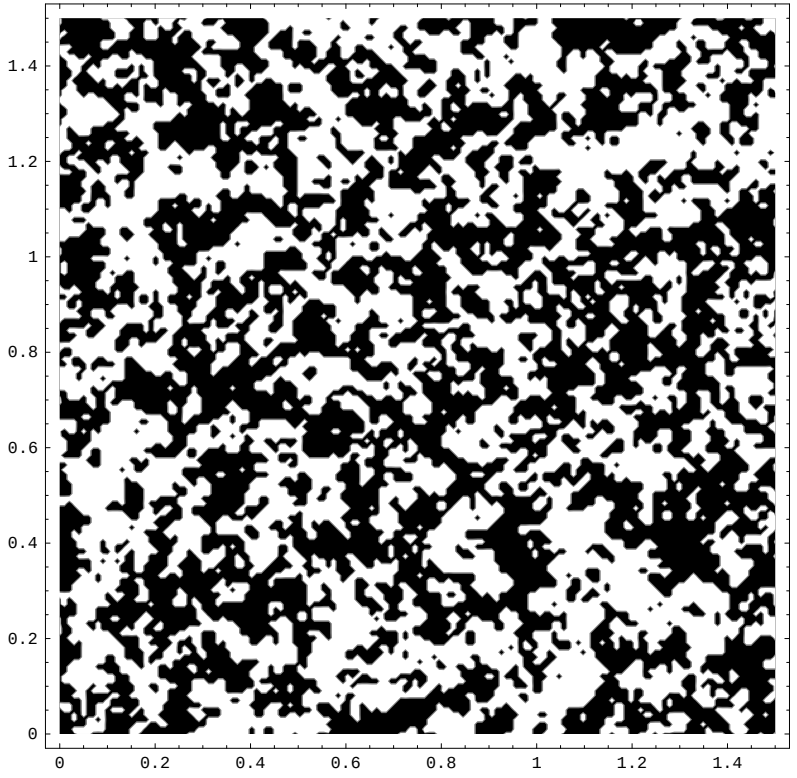

GH saturation distribution. White zones correspond to S_{gh} =0.9, while black zones represent cells with $S_{gh} = 0.25$.

Snapshots of z-component of the solid matrix. The domain is a square of side length 150 cm.

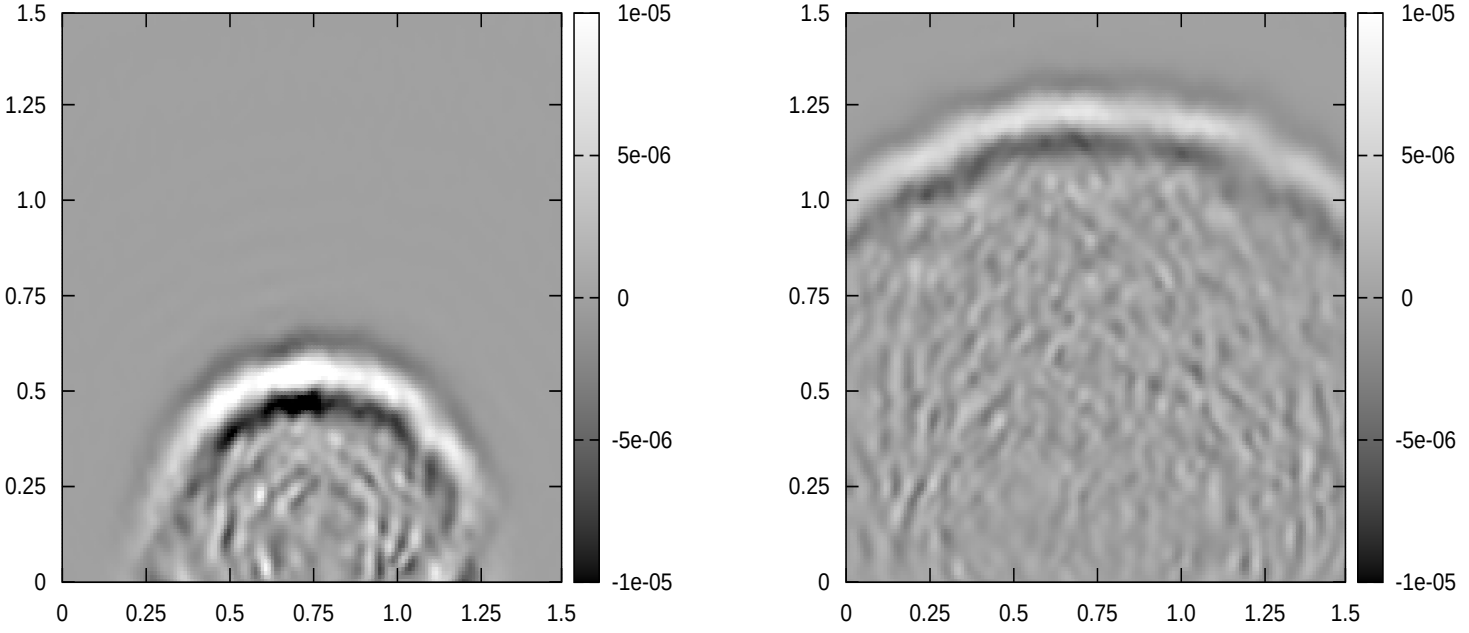

Snapshots of the z-component of the velocity of the solid matrix at $t = 0.25$ms and $t = 0.5$ms. A compressional point source of dominant frequency 10 kHz is located at $x = 75$ cm, $z = 10$ cm. Strong amplitude decays and conversions to slow compressional (P_2, P_3) and shear (S_2) waves are observed.

Snapshots of the divergence and curl of the solid matrix. The domain is a square of side length 150 cm.

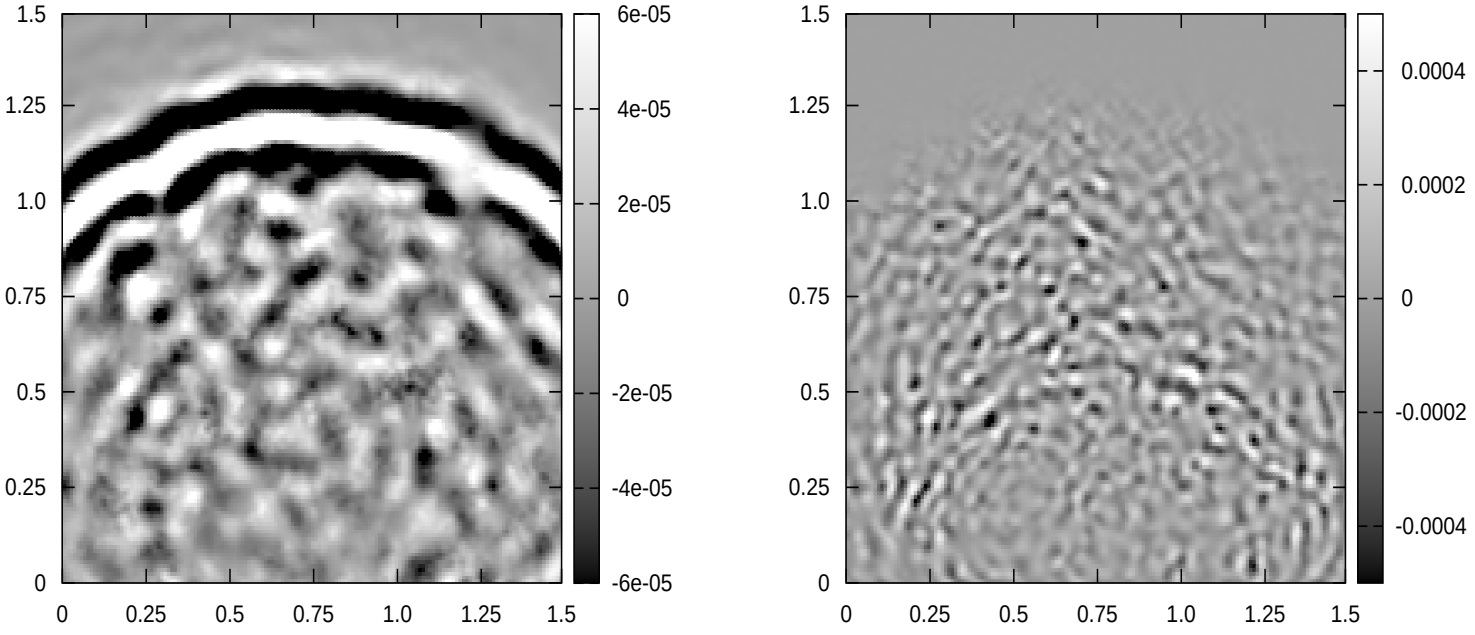

Snapshots of the divergence (left) and curl (right) of the velocity of the solid matrix at $t = 0.5$ms. The figures display the generation of slow compressional (P_2, P_3) and shear (S_2) waves due to energy conversions at the heterogeneities.

Time histories for the homogeneous (constant $S_{gh} = 0.58$) and heterogeneous cases.

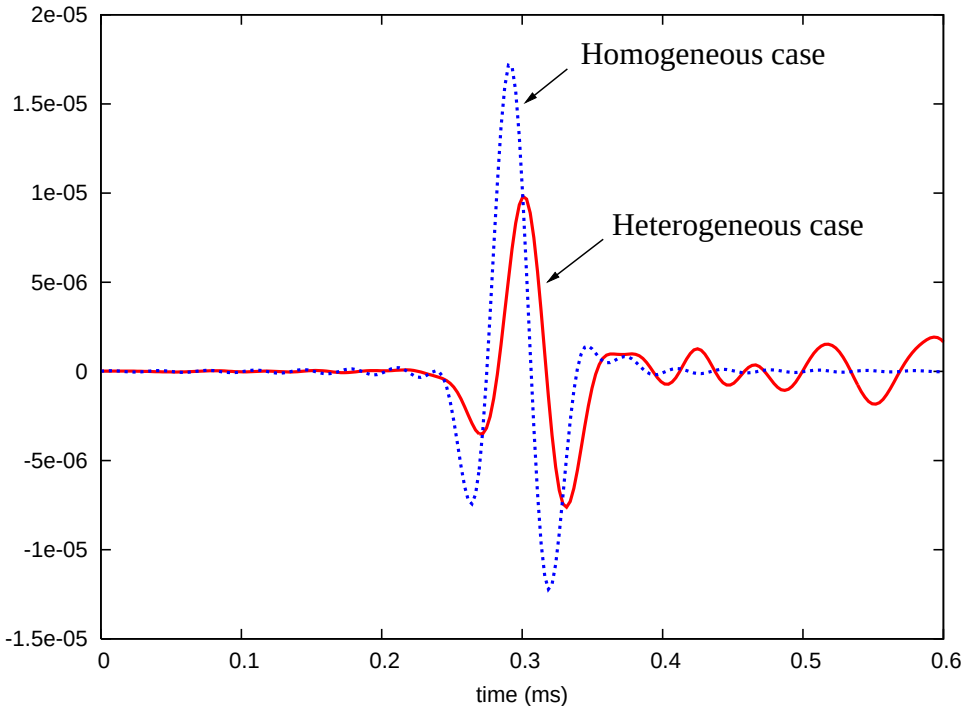

Time histories of the z-component of the particle velocity of the solid matrix for the homogeneous and heterogeneous cases at a receiver located at $x = 75$cm, $z = 70$cm. The amplitude peak corresponding to the arrival of the fast compressional P_1 wave in the heterogeneous case is much lower than in the homogeneous case due to energy conversions.

Time histories of waves travelling in highly heterogeneous GH bearing sediments

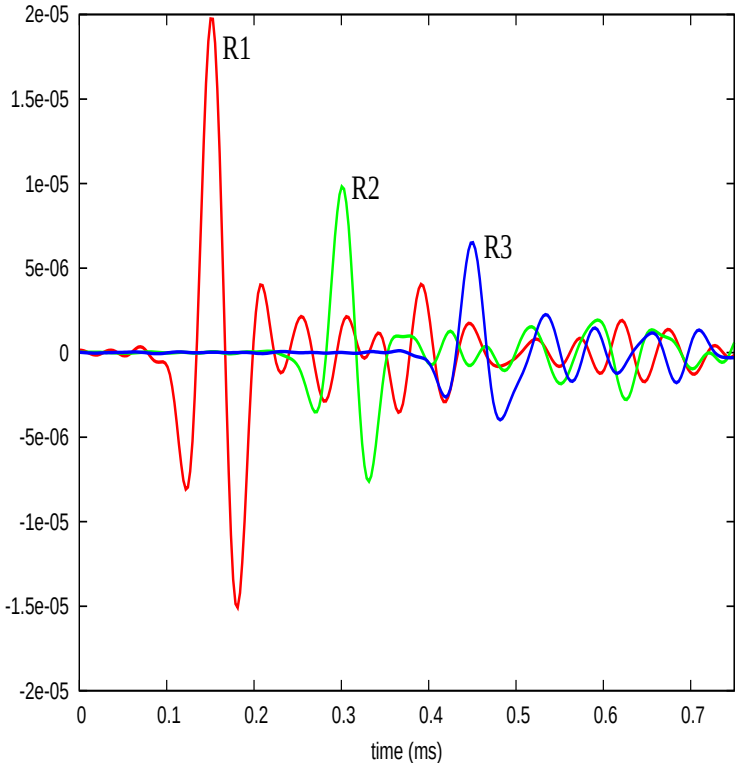

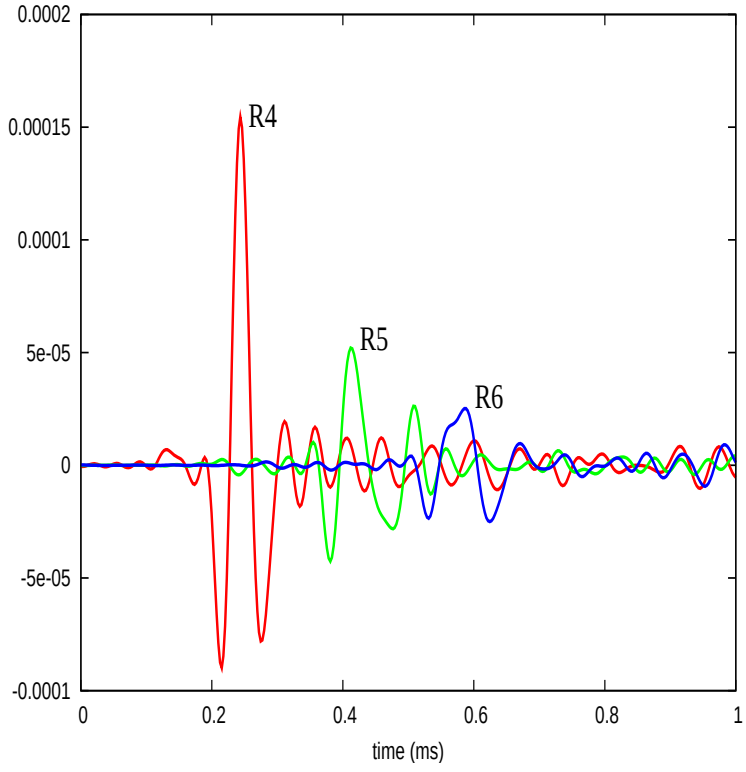

Time histories of the vertical (left) and horizontal (right) components of the velocity of the solid matrix at 3 receivers. The average quality factors: Q_p = 10.5 (from left) and Q_s = 5.5 (from right) are in excellent agrement with those measured at the Mallik 5L-38 GH Research Well.

Numerical simulations at the Mesoscale. I

- Due to the extremely fine meshes needed to properly represent very thin layers and other type of mesoscopic-scale heterogeneities, numerical simulations at the macroscale using Biot's equations are very expensive or even not feasible.
- In the contex of Numerical Rock Physics, we use a numerical upscaling procedure to determine the complex and frequency dependent stiffness of an equivalent TIV medium at the macroscale including the mesoscopic-scale effects.
- The methodology is illustrated for the case of a fluid-saturated porous rock containing parallel fractures.

Fractured induced anisotropy in porous media. The Mesoscale. II

- Seismic wave propagation through fractures is an important subject in hydrocarbon exploration geophysics, mining and reservoir characterization and production.
- Naturally fractured reservoirs have received interest in recent years, since, generally, natural fractures control the permeability of the reservoir.
- In geophysical prospecting and reservoir development, knowledge of fracture orientation, densities and sizes is essential since these factors control hydrocarbon production.
- This is also important in CO_2 storage in geological formations to monitor the injected plumes as faults and fractures are generated, where CO_2 can leak to the surface.

Fractured induced anisotropy in porous media. The Mesoscale. III.

- A planar fracture embedded in a fluid-saturated poroelastic background is a particular case of the thin layer problem, when one of the layers is very thin and compliant.
- A dense set of horizontal fractures in a fluid-saturated poroelastic medium behaves as a Transversely Isotropic Viscoelastic (TIV) medium when the average fracture distance is much smaller than the predominant wavelength of the traveling waves.
- Wave anelasticity and anisotropy are significant in fractured poroelastic rocks due to conversion of fast compressional waves into diffusion-type Biot slow waves.
- This leads to frequency and angular variations of velocity and attenuation of seismic waves.

The constitutive relations of a TIV media.

τ_{ij}: stress tensor of the equivalent TIV medium

For a **closed system**($\nabla \cdot u^f = 0$), the corresponding **stress-strain relations**, stated in the space-frequency domain, are

$$\begin{aligned}
\tau_{11}(u) &= p_{11}\,\epsilon_{11}(u^s) + p_{12}\,\epsilon_{22}(u^s) + p_{13}\,\epsilon_{33}(u^s),\\
\tau_{22}(u) &= p_{12}\,\epsilon_{11}(u^s) + p_{11}\,\epsilon_{22}(u^s) + p_{13}\,\epsilon_{33}(u^s),\\
\tau_{33}(u) &= p_{13}\,\epsilon_{11}(u^s) + p_{13}\,\epsilon_{22}(u^s) + p_{33}\,\epsilon_{33}(u^s),\\
\tau_{23}(u) &= 2\,p_{55}\,\epsilon_{23}(u^s),\\
\tau_{13}(u) &= 2\,p_{55}\,\epsilon_{13}(u^s),\\
\tau_{12}(u) &= 2\,p_{66}\,\epsilon_{12}(u^s).
\end{aligned}$$

This relations provide the complex velocities of the fast modes and takes into account **interlayer flow effects**.

To determine the complex stiffness we solve Biot's equation in the 2D case on a reference square $\Omega = (0, L)^2$ with boundary Γ in the (x, z)-plane. Set $\Gamma = \Gamma^L \cup \Gamma^B \cup \Gamma^R \cup \Gamma^T$, where

$$\Gamma^L = \{(x, z) \in \Gamma : x = 0\}, \quad \Gamma^R = \{(x, z) \in \Gamma : x = L\},$$

$$\Gamma^B = \{(x, z) \in \Gamma : z = 0\}, \quad \Gamma^T = \{(x, z) \in \Gamma : z = L\}.$$

The harmonic experiments to determine the stiffness coefficients. II

The sample is subjected to harmonic compressibility and shear tests described by the following sets of boundary conditions.

$p_{33(\omega)}$:

$$\sigma(u)\nu \cdot \nu = -\Delta P, \quad (x,z) \in \Gamma^T,$$
$$\sigma(u)\nu \cdot \chi = 0, \quad (x,z) \in \Gamma^T \cup \Gamma^L \cup \Gamma^R,$$
$$u^s \cdot \nu = 0, \quad (x,z) \in \Gamma^L \cup \Gamma^R,$$
$$u^s = 0, \quad (x,z) \in \Gamma^B, \quad u^f \cdot \nu = 0, \quad (x,z) \in \Gamma.$$

ν: the unit outer normal on Γ

χ: a unit tangent on Γ so that $\{\nu, \chi\}$ is an orthonormal system on Γ.

Denote by V the original volume of the sample and by $\Delta V(\omega)$ its (complex) oscillatory volume change.

The harmonic experiments to determine the stiffness coefficients. III

In the quasistatic case

$$\frac{\Delta V(\omega)}{V} = -\frac{\Delta P}{p_{33}(\omega)},$$

Then after computing the average $u_z^{s,T}(\omega)$ of the vertical displacements on Γ^T, we approximate

$$\Delta V(\omega) \approx L u_z^{s,T}(\omega)$$

which enable us to compute $p_{33}(\omega)$

The other coefficients are determined measuring changes in volume or shape of the sample.

Schematic representation of the oscillatory compressibility and shear tests in Ω

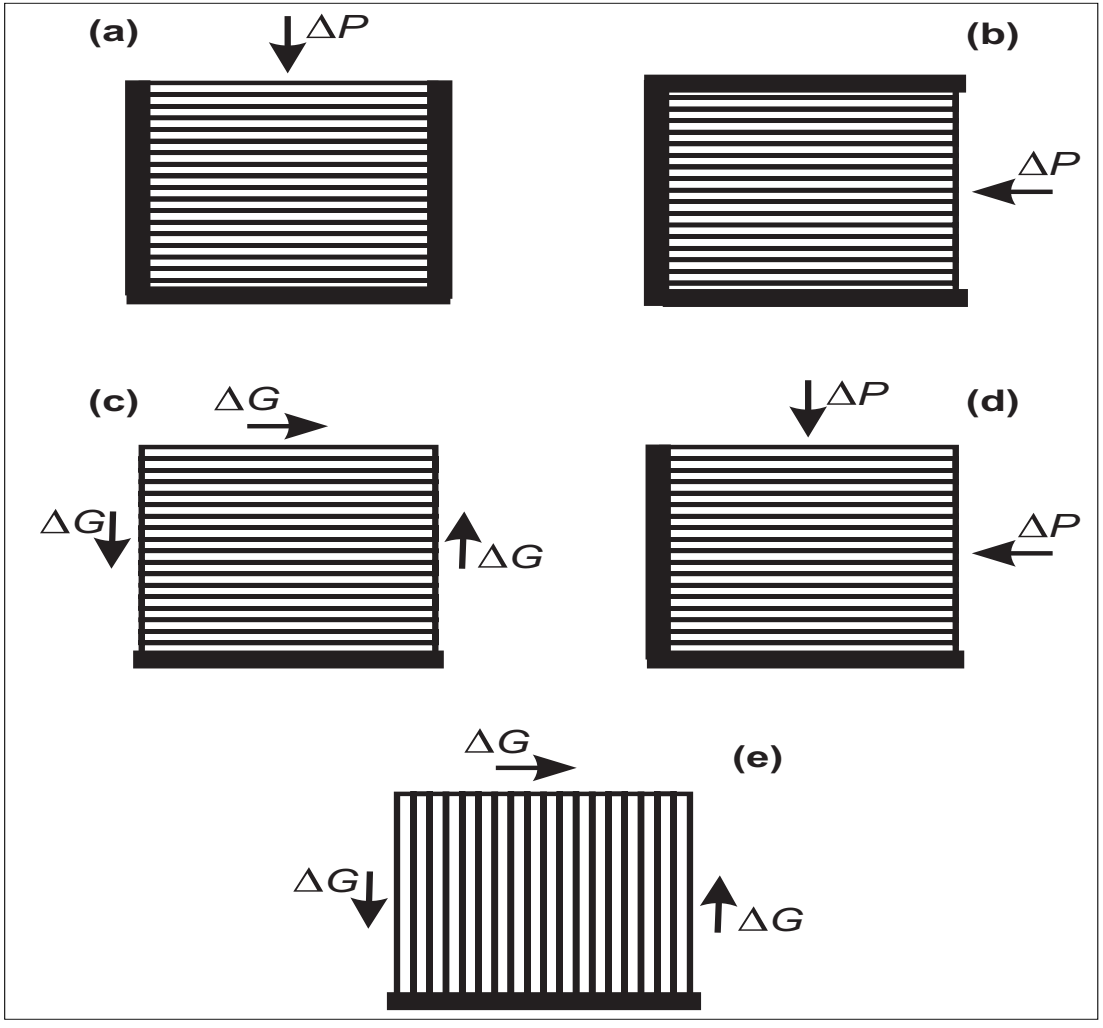

a): p_{33}, b): p_{11}, c): p_{55}, d): p_{13} e): p_{66}

Examples. I

A set of numerical examples consider the following cases for a square poroelastic sample of 160 cm side length and 10 periods of 1 cm fracture, 15 cm background:

- **Case 1: A brine-saturated sample with fractures.**
- **Case 2: A brine-CO_2 patchy saturated sample without fractures.**
- **Case 3: A brine-CO_2 patchy saturated sample with fractures.**
- **Case 4: A brine saturated sample with a fractal frame and fractures.**

Examples. II

- **The discrete BVP's to determine the complex stiffnesses $p_{IJ}(\omega)$ were solved for 30 frequencies using a public domain sparse matrix solver package.**
- **Using relations not included for brevity, the $p_{IJ}(\omega)$'s determine in turn the energy velocities and dissipation coefficients shown in the next figures.**

Polar representation of the qP energy velocity vector at 50 Hz for cases 1, 2 and 3

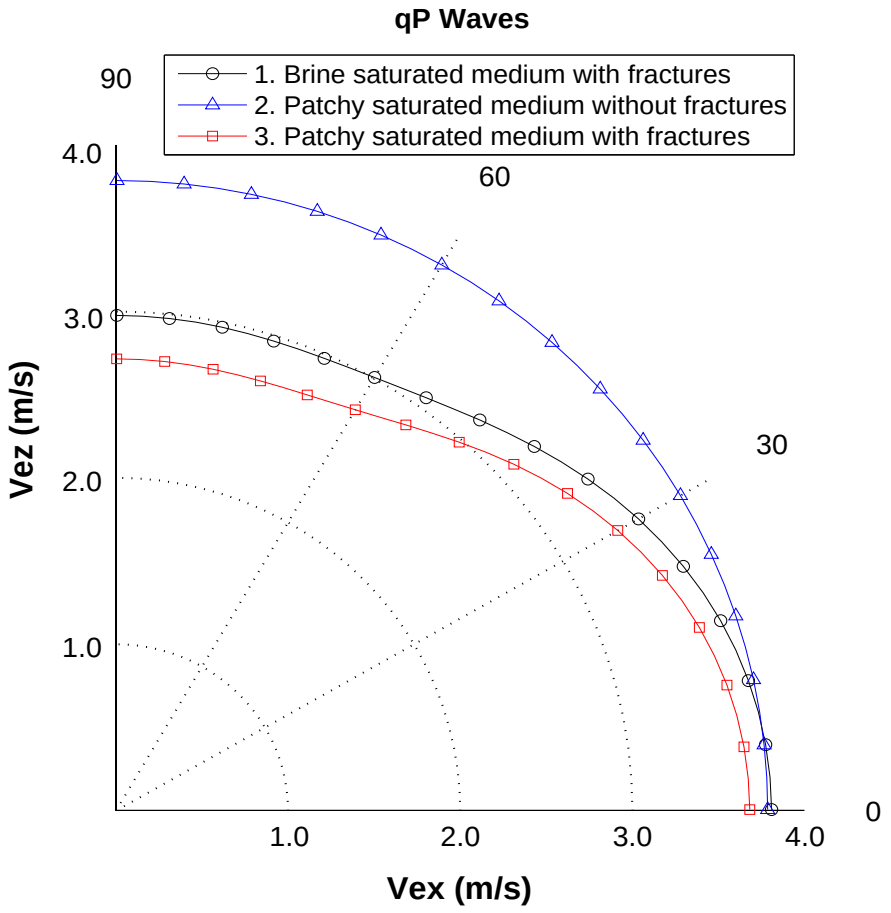

Velocity anisotropy caused by the fractures in cases 1 and 3 is enhanced for the case of patchy saturation, with lower velocities when patches are present. The velocity behaves isotropically in case 2.

Dissipation factor of the qP waves at 50 Hz for cases 1, 2 and 3

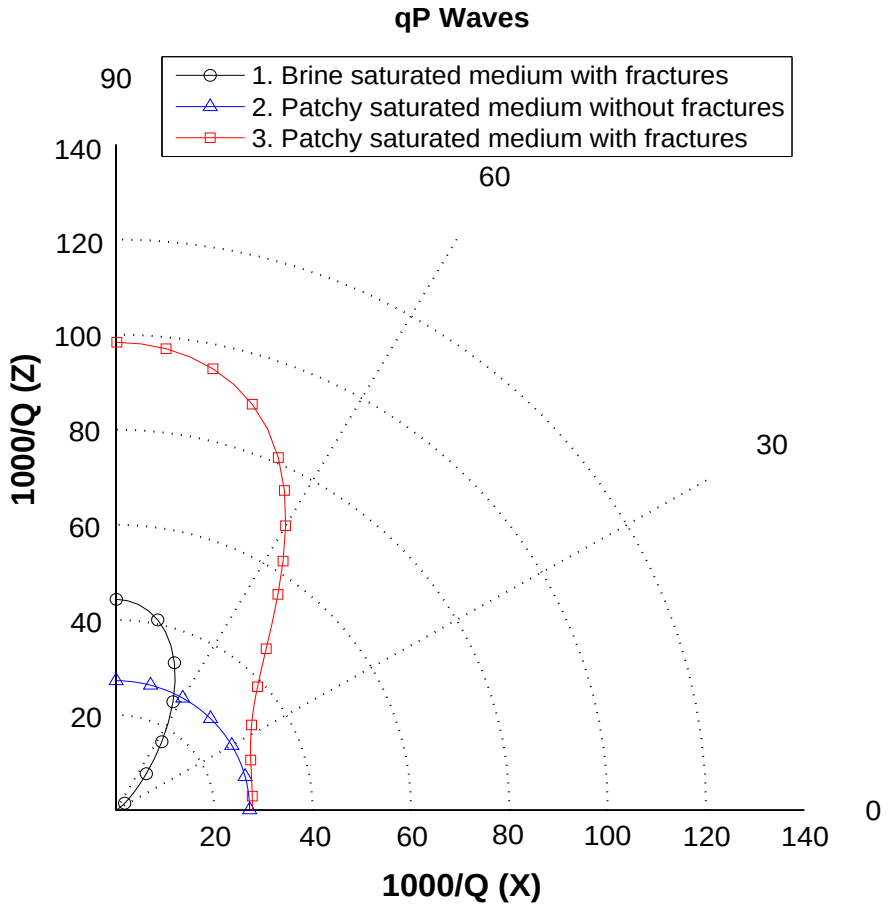

Fractures induce strong Q anisotropy for angles normal to the fracture plane, enhanced by patchy saturation.

Fluid pressure distribution at 50 and 300 Hz. Compressibility test for p_{33} for case 3.

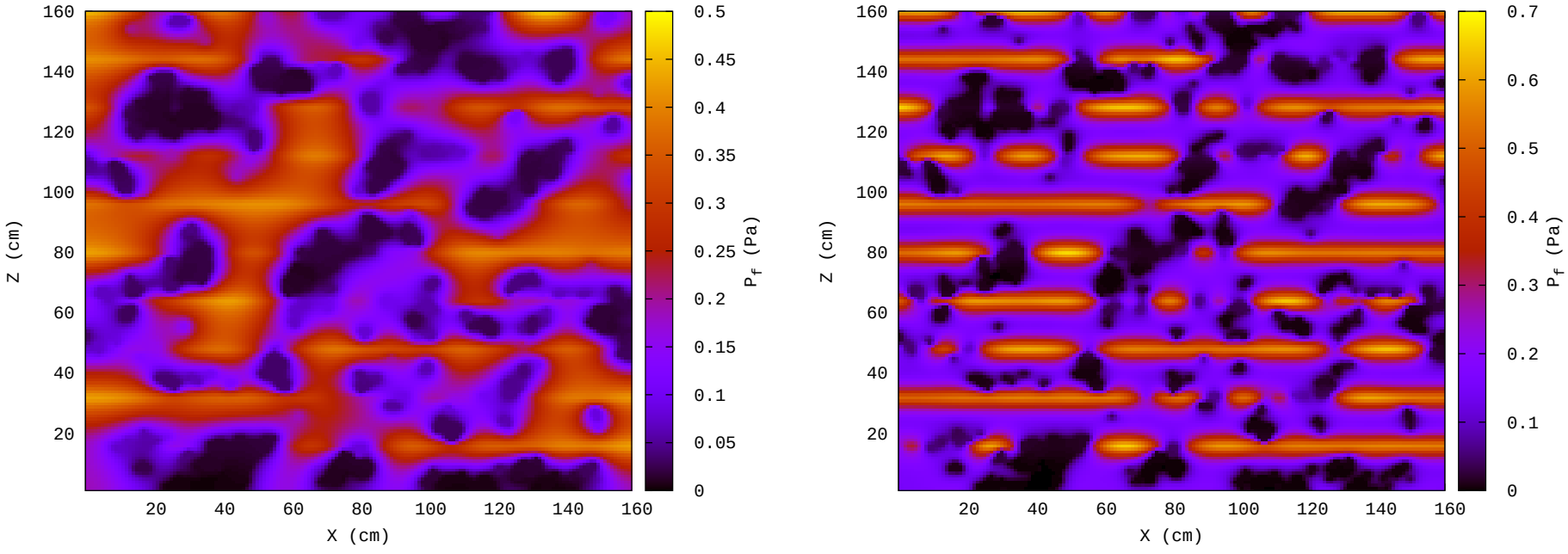

Compression is normal to the fracture plane. Attenuation is stronger at 300 Hz.

Polar representation of the qSV energy velocity vector at 50 Hz for cases 1, 2 and 3

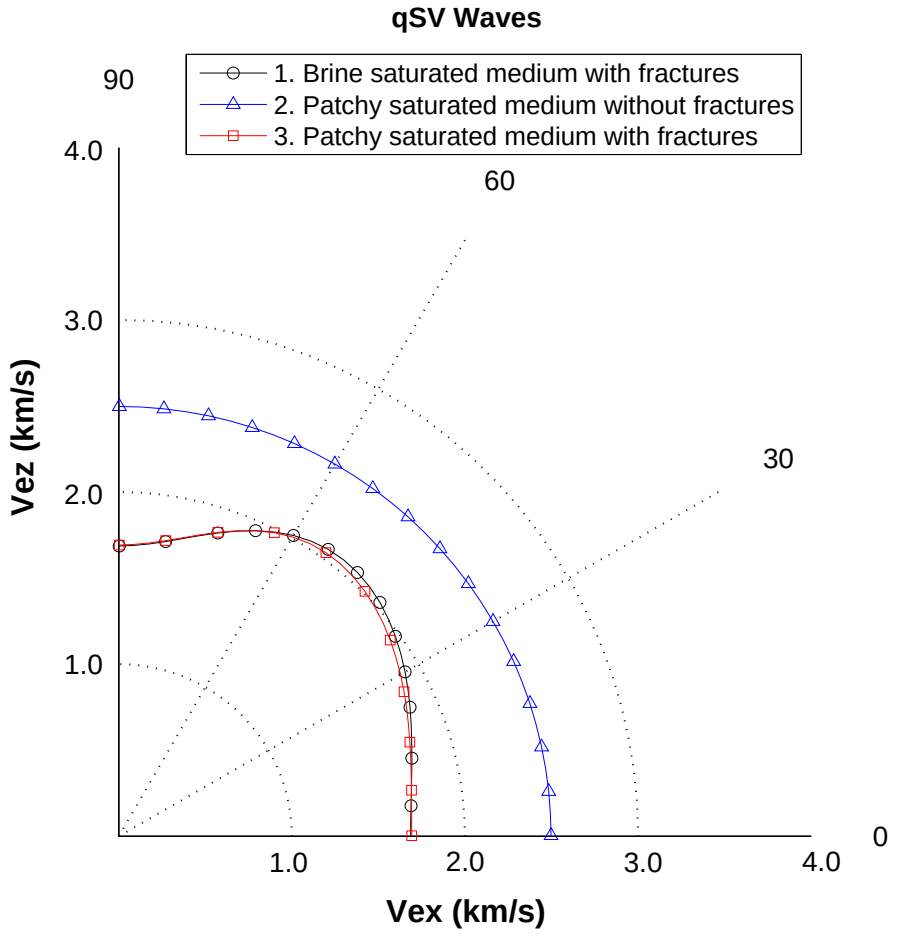

Velocity anisotropy is induced by fractures (cases 1 and 3). Patchy saturation does not affect the anisotropic behavior of the qSV velocities. Case 2 shows isotropic velocity, with higher velocity values than for the fractured cases

Dissipation factor of qSV waves at 50 Hz for cases 1, 2 and 3

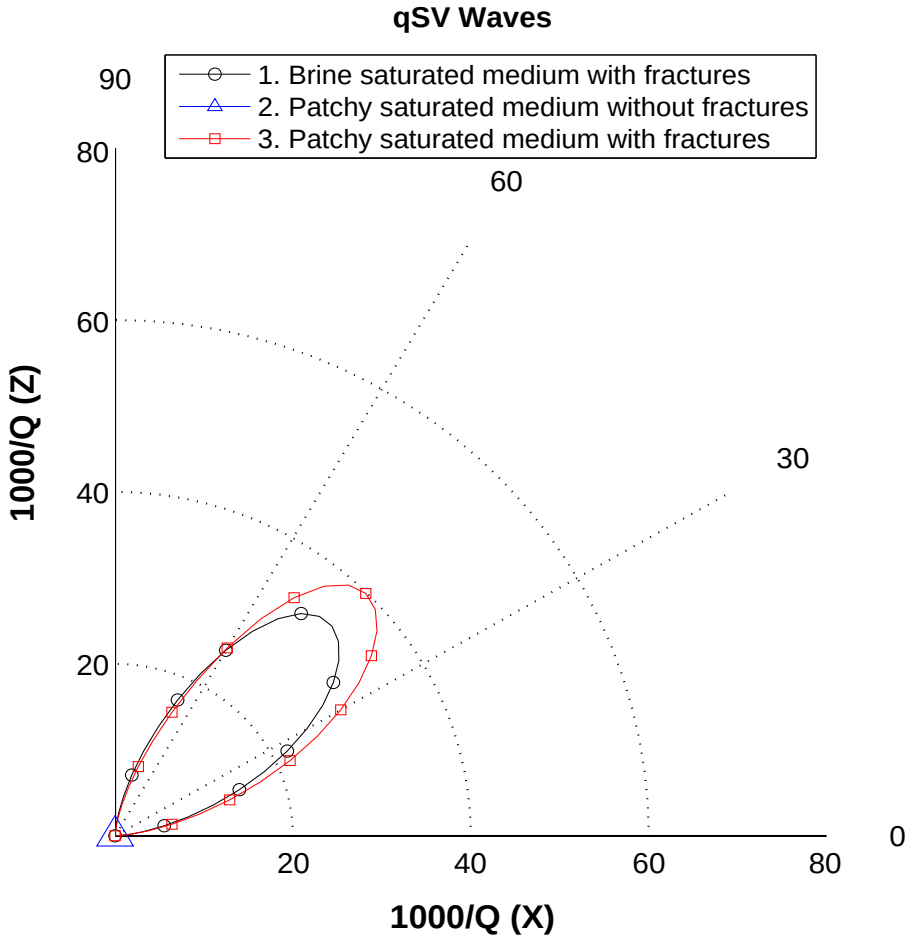

qSV anisotropy is strong for angles between 30 and 60 degrees. The lossless case 2 is represented by a triangle at the origin

Polar representation of the qSH energy velocity vector at 50 Hz for cases 1, 2 and 3

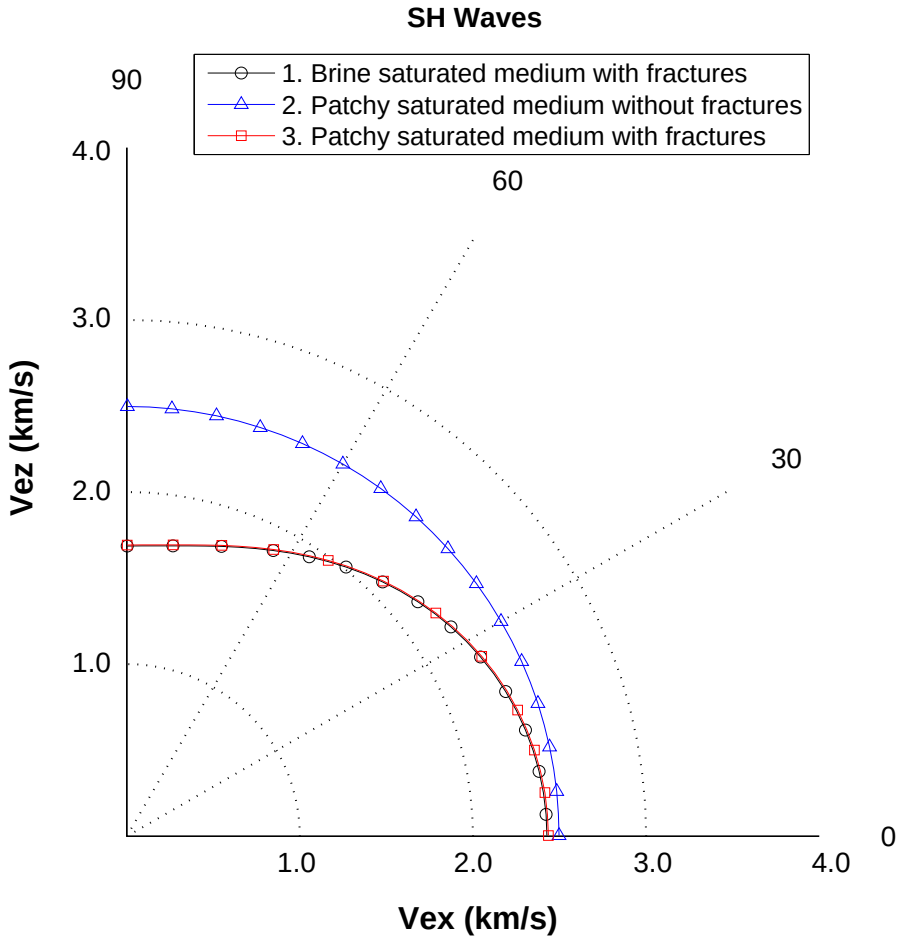

SH velocity anisotropy is observed to be induced by fractures. Cases 1 and 3 are almost indistinguishable. Velocity for case 2 is isotropic. SH waves are lossles, since p_{55} and p_{66} are real.

Lamé coefficient (GPa) for the brine-saturated fractal porosity-permeability sample of case 4.

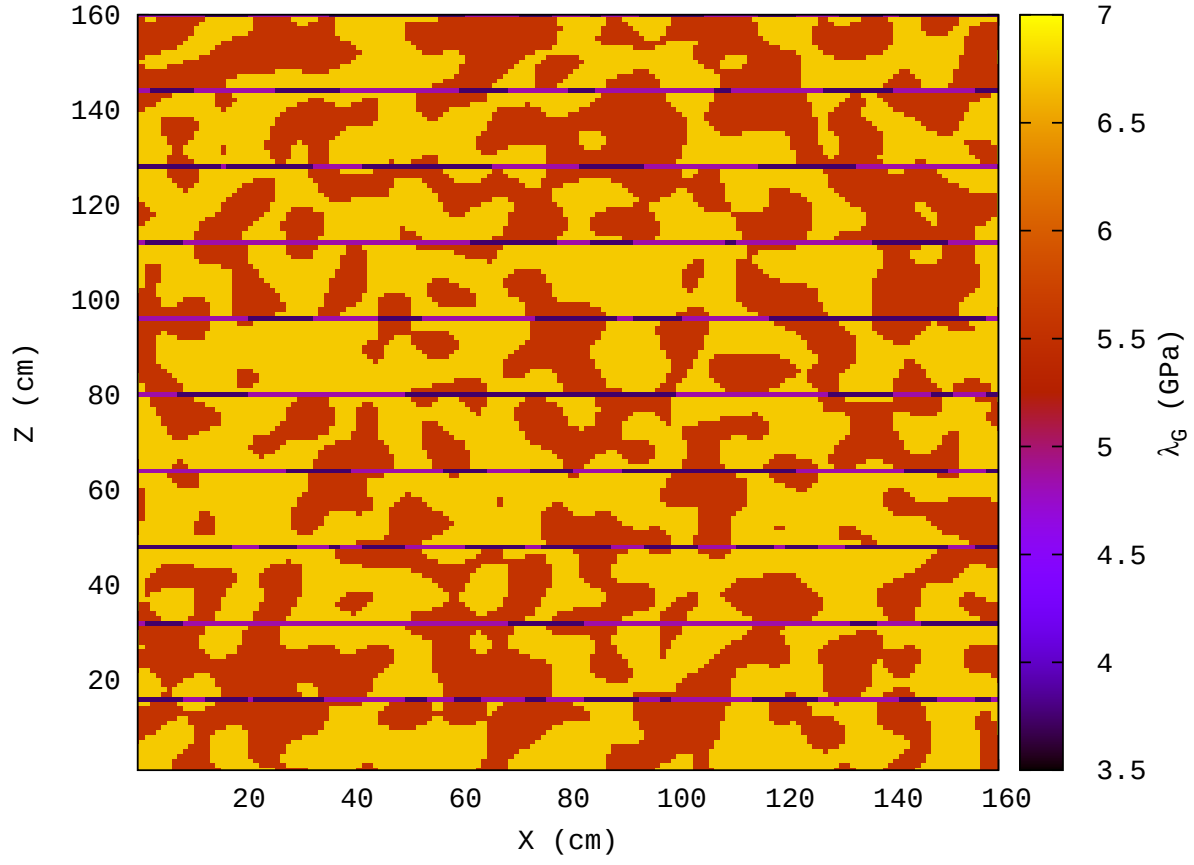

log $\kappa(x,z) = \langle \log \kappa \rangle + f(x,z)$, $f(x,z)$: fractal representing the spatial fluctuation of the permeability field $\kappa(x,z)$. Porosity was obtained using the Kozeny-Carman relation. The Lamé coefficients were computed using a Krief model.

Dissipation factor of qP waves at 50 Hz for cases 1 and 4.

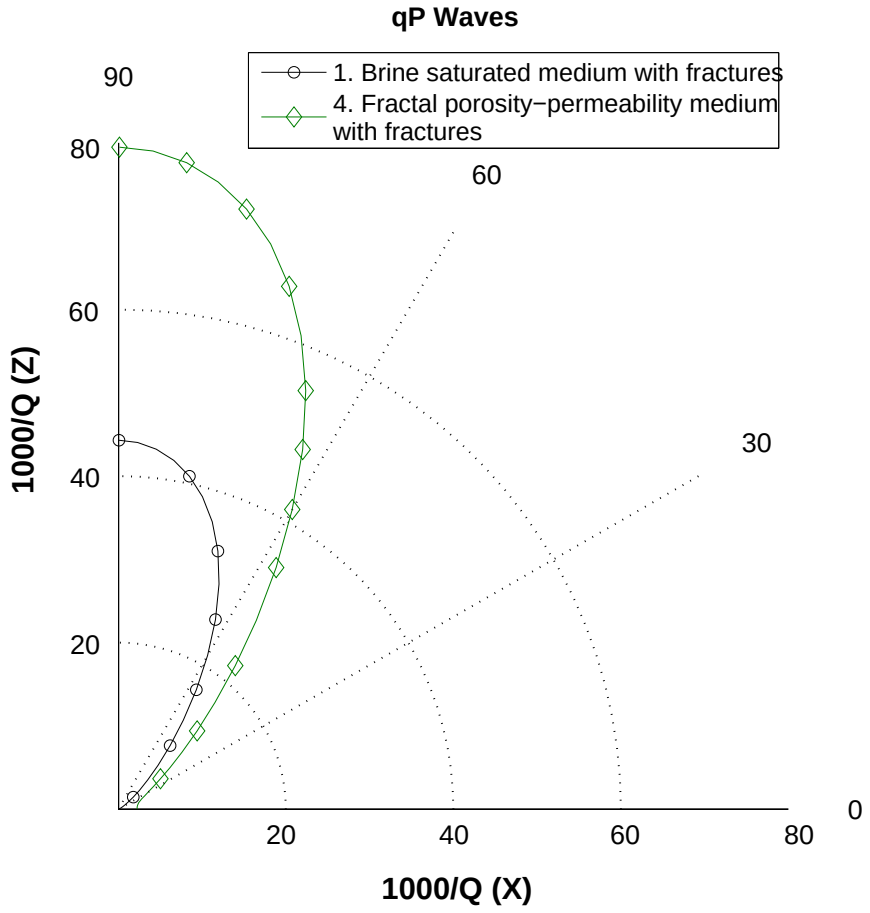

Note the increase in Q anisotropy for qP waves for angles normal to the fracture plane.

Dissipation factor of qSV waves at 50 Hz for cases 1 and 4.

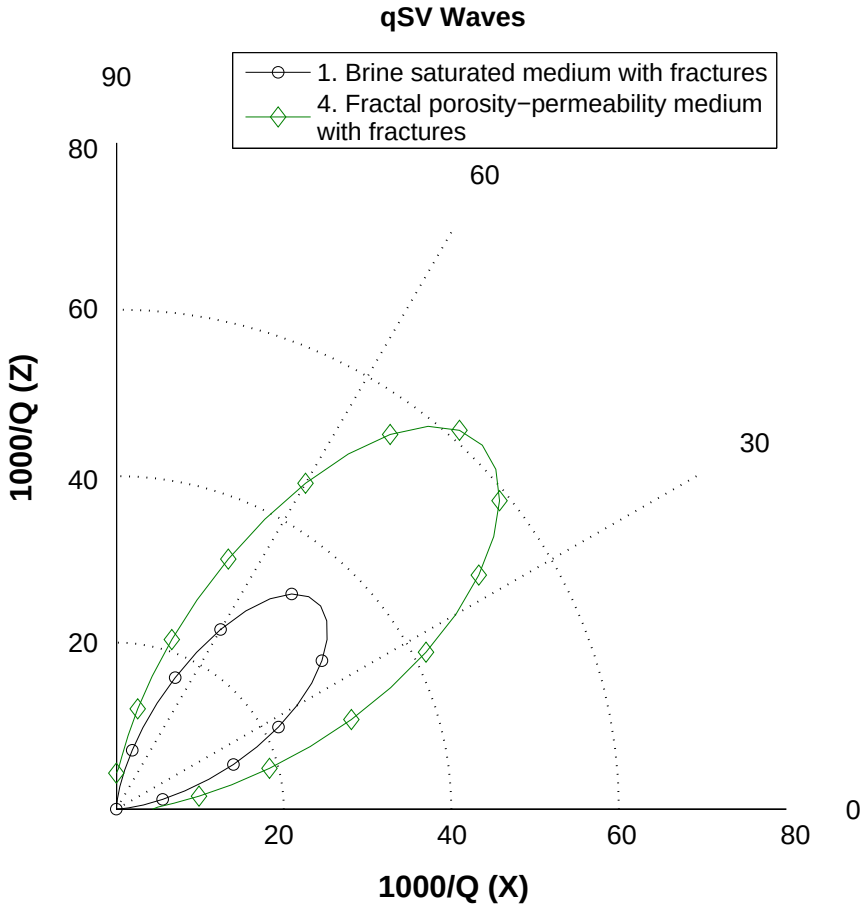

Note the increase in Q anisotropy for angles between 30 and 60 degrees

The Macroscale. I.

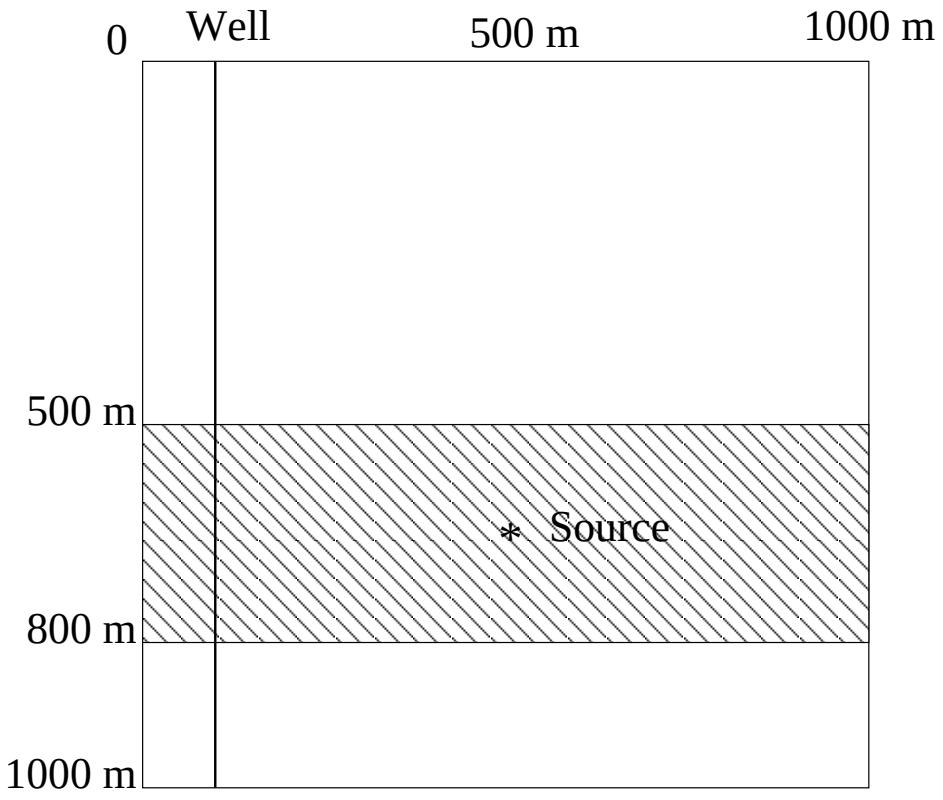

The Macroscopic TIV model: an anisotropic rotated TIV layer between two isotropic half-spaces. The source is a dilatational perturbation of central frequency is 30 Hz

The Macroscale. II. Seismic modeling.

We solve the following boundary value problem at the macroscale (in Ω):

$$-\omega^2 \rho u - \nabla \cdot \tau(u) = F, \quad \Omega$$

$$-\tau(u)\nu = i\omega \mathcal{D} u, \quad \partial\Omega, \text{ (absorbing bounday condition, } D > 0\text{)}$$

$u = (u_x, u_z)$: **displacement vector,** ρ: **average density.**

$\tau(u)$: **stress-tensor of our equivalent viscoelastic material, defined in terms of the** $p'_{IJ}s$**, obtained using the upscaling procedure.**

We solved this problem employing a FE iterative domain decomposition technique formulated in the space-frequency domain.

The Macroscale. III. Snapshots of the vertical displacement at 200 ms (a and c) and 500 ms (b and d).

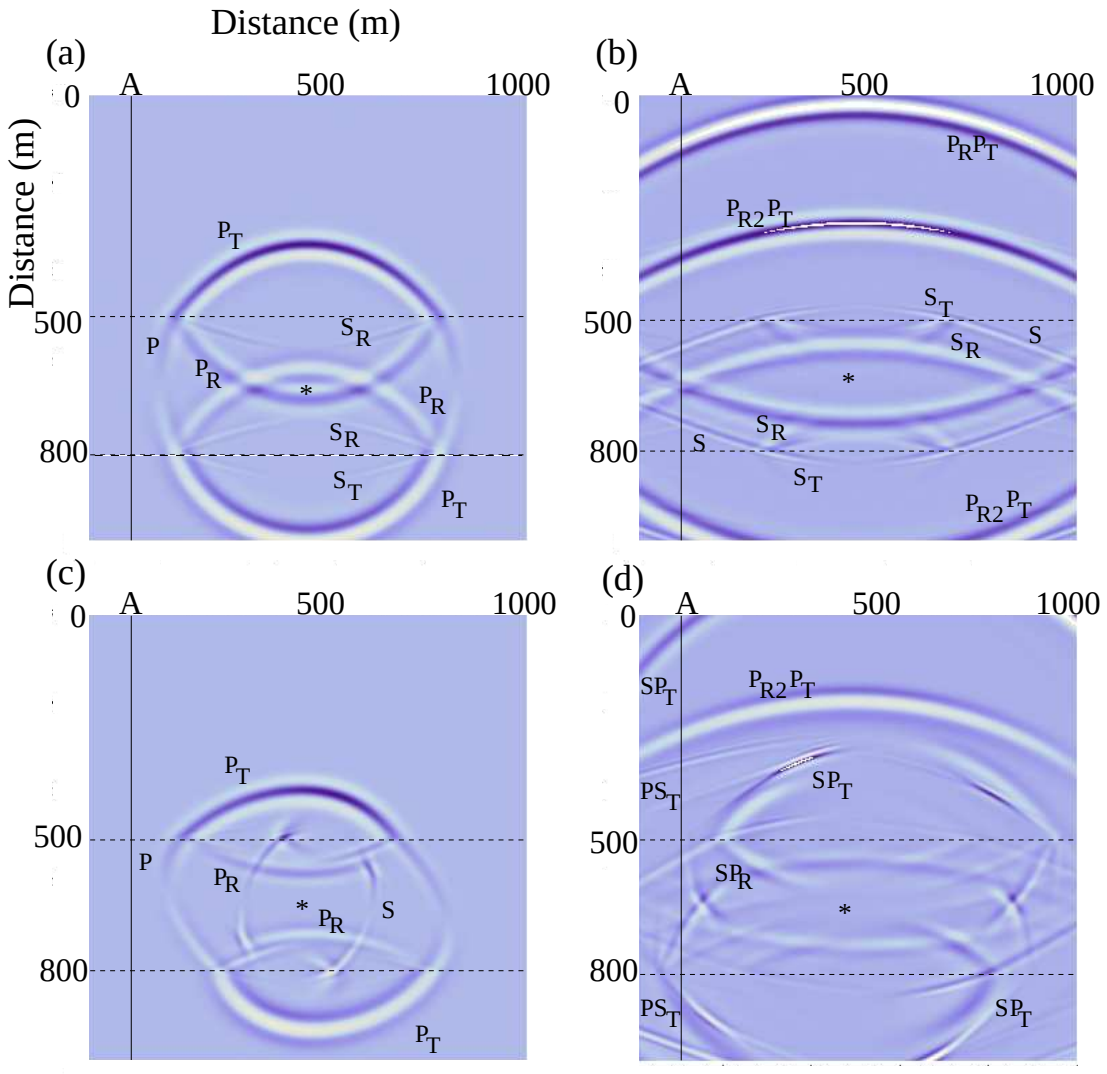

Ideal isotropic case (top, a and b) and real (rotated TIV) case (bottom, c and d).

Conclusions

- Numerical simulation is a useful tool in hydrocarbon exploration geophysics, mining and reservoir characterization and production.
- The FEM allows to analyze and represent mesoscopic scale heterogeneities in the solid frame and saturant fluids, fractures and craks affecting observations at the macroscale.
- Wave propagation at the macroscale can be efficiently performed employing the FEM combined with iterative domain decomposition techniques formulated in the space-frequency domain.
- The ideas presented here to model acoustics of porous media can be extended to other fields, like ultrasound testing of quality of foods, groundwater flow and contamination among others.
- Thanks for your attention !!!!!.